ROYAL SOCIETY OF CHEMISTRY

PAPER

Efficient hydrogen evolution at Ni/CeOx interfaces in anion-exchange membrane water electrolysers†

Ibrahem O. Baibars, ‡[a] Haisen Huang,‡[b] Yang Xiao,[a] Shuhao Wang,[a] Yan Nie,[a] Chen Jia, [a] Kamran Dastafkan [a] and Chuan Zhao ★[a]

A macro/mesoporous film with Ni/CeOx interfaces is designed *via* the dynamic hydrogen bubble template (DHBT) method for ampere-level production of hydrogen in anion exchange membrane water electrolysers (AEMWEs). The AEMWE achieves leading energy efficiencies of 95% and 80%, based on the higher and lower heating values of hydrogen, respectively, at 0.25 A cm^{-2}, producing hydrogen at 42 kW h kg^{-1} and a cost of $0.84 per kg, thereby meeting the U.S. Department of Energy (DOE) price target ($1 per kg) for 2030. A current density of 5 A cm^{-2} is achieved at 2.08 V and 60 °C in the AEMWE, with overall cell activation and concentration overpotentials of 594 mV, establishing a leading position in the field. The Ni/CeOx catalyst exhibits superb hydrogen evolution reaction (HER) activity by delivering 1 A cm^{-2} at an overpotential of 201 mV at 20 °C, far surpassing Ni, CeOx, and benchmark Pt/C catalysts. Electrochemical and theoretical calculations reveal accelerated charge transfer due to the preferential adsorption of intermediates at the tailored defective interfaces during hydrogen evolution. Hydrogen evolving during electro-deposition forms 3D channels for bubble removal in the AEMWE, akin to a hydrogen memory, speeding up mass transfer.

Broader context

Overpotential sources, particularly activation and concentration overpotentials, represent a major barrier to achieving high efficiency in anion exchange membrane water electrolysers (AEMWEs), significantly limiting their real-world performance. A Ni/CeOx heterostructure catalyst with a hierarchical macro/mesoporous morphology is designed to address both overpotentials. The defective interfaces synergistically accelerate charge transfer by promoting water dissociation, hydroxide desorption, and hydrogen adsorption, while the hierarchical pores mitigate mass transfer limitations through improved electrolyte and bubble transport. This design enables the AEMWE to achieve remarkable performance metrics, including a hydrogen generation current density of 5 A cm^{-2} at 2.08 V and 60 °C with a total overpotential of 594 mV, and energy efficiencies of 95% and 80% (based on higher and lower heating values, respectively) at 0.25 A cm^{-2}. The hydrogen production cost is reduced to $0.84 per kg, surpassing the U.S. Department of Energy's (DoE) target of $1 per kg by 2030. By combining advanced catalyst design with a robust framework for analysing overpotential sources, this work not only meets critical efficiency and cost targets but also establishes a foundation for further optimization and scalability in green hydrogen production.

Introduction

Hydrogen production *via* water electrolysis is a promising green energy solution, enabling grid-level electricity storage and on-demand energy supply.[1] Anion exchange membrane water electrolysers (AEMWEs) combine the advantages of current commercial technologies, *i.e.*, proton exchange membranes (PEMs) and alkaline water electrolysers (AWEs), and operate in mild alkaline media with minimized carbonate formation and lower corrosivity, allowing the use of noble-metal-free catalysts.[2,3] The zero-gap design of AEMWEs with compact membrane electrode assembly (MEA) also offers minimized ohmic resistance, allowing for high-purity hydrogen production at high current densities.[2,4] Importantly, AEMWEs can take advantage of the existing infrastructures of AWEs and PEMWEs for scaled catalyst and MEA manufacturing, making them very promising for commercialisation. However, to achieve hydrogen production costs comparable to steam reforming, AEMWE systems require further advancements in

[a] *School of Chemistry, The University of New South Wales, Sydney, NSW, 2052, Australia. E-mail: chuan.zhao@unsw.edu.au*

[b] *CAS Key Laboratory of Materials for Energy Conversion, Department of Materials Science and Engineering, University of Science and Technology of China, Hefei, Anhui, 230026, P. R. China*

† Electronic supplementary information (ESI) available. See DOI: **https://doi.org/10.1039/d4ee06113f**

‡ These authors contributed equally to this work.

energy efficiency and reductions in capital and operational expenditures.[5,6]

Energy efficiencies of water electrolysers are typically governed by three types of overpotentials: activation overpotential (including chemical and charge transfer), concentration overpotential (mass transfer), and ohmic overpotential.[7,8] The ohmic overpotential is primarily ionic, influenced by the membrane type and thickness, provided that electronic contributions from catalysts and other cell components are minimized through appropriate design and assembly.[4] While AEMWEs benefit from faster oxygen evolution (OER) kinetics in alkaline solutions, the hydrogen evolution reaction (HER) is retarded due to the scarcity of H^{+} ions, which requires a prerequisite water dissociation step followed by hydroxide removal, resulting in extra energy barriers and a further increase in activation overpotentials.[9,10] To overcome these activation overpotentials, various catalyst designs have been developed, including high-entropy alloys,[11] single-atom catalysts,[12] heteroatom-doped catalysts,[13,14] and defect-rich catalysts.[15] Among these designs, heterostructured catalysts show great synergy potential at the interfaces formed between a wide range of materials.[16,17] Thirdly, concentration overpotential is controlled by mass transfer to (for electrolyte) and from (for gas bubbles) the catalyst surface. At high current densities, concentration overpotential becomes more pronounced due to the increased demand for the electrolyte and the blockage of active sites by numerous bubbles.[18] Catalyst morphology is therefore crucial for preventing the accumulation and coalescence of gas bubbles, improving electrolyte accessibility, and minimizing the concentration overpotential.[8,19,20]

Here, a heterostructured Ni/CeO$_x$ catalyst is designed to minimize the activation overpotential *via* interfacial synergy that facilitates water dissociation and provides suitable sites for the adsorption of H and desorption of OH^{−} and H$_2$. Metal/metal oxide heterostructures have been reported to speed up HER kinetics in alkaline media.[21-23] CeO$_2$ is known for non-stoichiometry, O vacancy abundance, facile Ce^{3+}/Ce^{4+} transition, and effective catalysis features *via* disrupting chemical bonds in reactants and intermediates at its defective sites.[24-27] Theoretical calculations, herein, reveal that CeO$_x$ sites help polarise water molecules, host OH^{−} ion desorption, and modulate Ni adsorption of H. Additionally, a highly porous Ni/CeO$_x$ catalyst layer is achieved *via* dynamic hydrogen bubble template (DHBT) electrodeposition.[28] During the deposition, catalyst layers grow around the co-produced hydrogen bubbles, forming hierarchical macro/meso-pores with nano-edges along the tracks of the bubbles.[28,29] These pores born from gas bubbles during catalyst synthesis are crucial for bubble removal and electrolyte access in MEA.[30] Catalyst/membrane interfaces are also enriched by the tortuosity of the catalyst clusters between pores, accelerating electrolyte delivery and minimizing mass transfer resistance. The designed Ni/CeO$_x$ film shows minimum mass transfer overpotential and low charge transfer overpotential when tested for the HER in a half-cell, a two-electrode electrolysis cell, and AEMWEs using different membranes.

Results and discussion

Synthesis and characterization

The design of a macro/mesoporous catalyst layer with Ni/CeO$_x$ interfaces using the DHBT method is grounded in several considerations. Firstly, while Ni films with hierarchical macropores have been deposited *via* DHBT,[31,32] similar morphologies for CeO$_x$ films have not been reported, likely due to deposition dependence on dissolved O$_2$[33] (see the deposition faradaic efficiency section in the ESI†). Therefore, a balance should be considered when determining the molar ratio of Ni^{2+} to Ce^{3+} in the deposition bath as the desire to increase the Ce content in the designed catalyst leads to losing the uniform macroporosity. Secondly, (NH$_4$)$_2$SO$_4$-based deposition baths are chosen over NH$_4$Cl and H$_2$SO$_4$ baths, commonly used in DHBT, to avoid chlorine gas evolution and undesired morphologies.[28,34] Thirdly, the applied deposition current density plays a key role in determining the resulting morphology and structure.[35]

In this study, various Ni/CeO$_x$ HER catalysts are fabricated on Ni foam substrates using a deposition bath with a Ni^{2+} to Ce^{3+} molar ratio of 9:1 by varying the applied current density and deposition times to maintain the same passing charge. The best-performing HER catalyst is found to be deposited at 2 A cm^{−2} (Fig. 1 and Fig. S15b, ESI†). Ni/CeO$_x$ (2 A) shows several hierarchical cone-shaped macropores with various diameters ranging from 16 μm down to 50 nm with tortuous cauliflower-like particles (Fig. 1b and Fig. S1a–c, ESI†). Both dark-field STEM and HRTEM images (Fig. 1c and d) show ∼60 nm-wide particles with mesopores of ∼10 nm diameter. The nitrogen adsorption isotherm from Brunauer–Emmett–Teller (BET) analysis illustrates the distribution of these mesopores, showing an average pore diameter of 7.4 nm (Fig. S2, ESI†). Additionally, the absence of a hysteresis loop indicates the ease of N$_2$ gas desorption and suggests fast H$_2$ bubble removal during the HER (Fig. S2a, ESI†). The wide variation in pore sizes, including macro and mesopores, reflects the diverse sizes of H$_2$ bubbles evolving during deposition. Such variations in pore sizes are crucial to accommodating the range of H$_2$ bubble sizes rising during water electrolysis, akin to a hydrogen memory.[30] SEM-EDS mapping analysis (Fig. S3, ESI†) shows the distribution of Ni, Ce, and O elements, with small oxygen content (9.97%), where O sites surround Ce sites in the overlay image, supporting the formation of Ce oxides interfaced with metallic Ni. Despite the quantification limitations of SEM-EDS, the resulting atomic ratio of Ni to Ce is 97:3, matching that obtained from ICP-OES (Table S1 and Fig. S3, ESI†). According to the ICP-OES data, deposition faradaic efficiency is calculated to be 7.78%, implying that 92.22% of the passing charge is consumed in producing hydrogen bubble templates (Fig. S4, ESI†). On the other hand, when Ni and CeO$_x$ components of the interface are deposited separately using the same method, the Ni film exhibits a macroporous morphology, while the CeO$_x$ film does not (Fig. S5–S8, ESI†). Four additional Ni/CeO$_x$ films are deposited at different current densities, resulting in two compact non-porous films at low current densities and two macroporous ones at high current densities, with the pore size
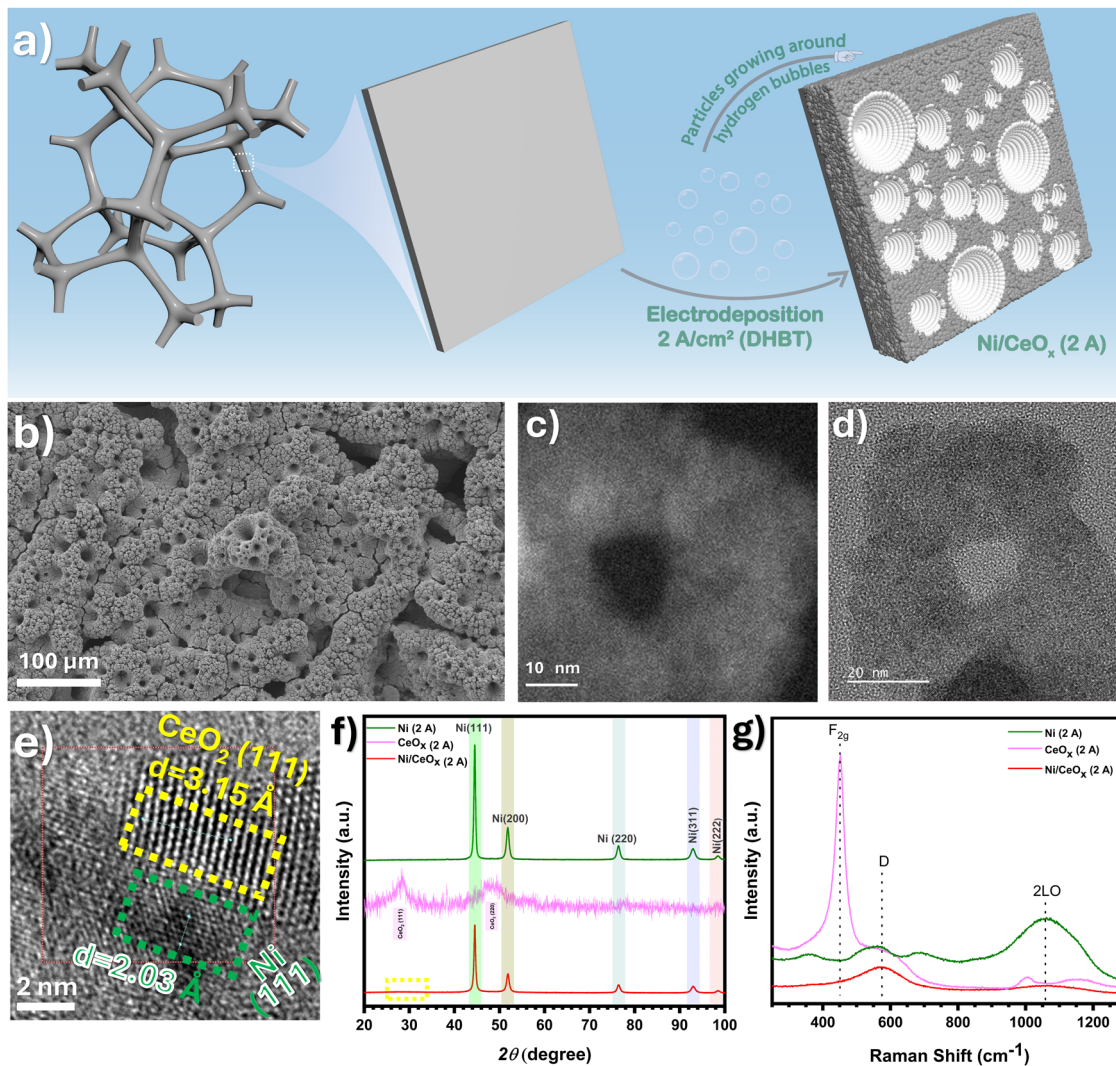
This journal is © The Royal Society of Chemistry 2025

Energy Environ. Sci., 2025, **18**, 6248–6259 | **6249**

Fig. 1 Synthesis, morphology, and structure. (a) A schematic representation of the synthesis of Ni/CeO$_x$ (2 A). (b) SEM, (c) dark-field STEM, (d) and (e) HR-TEM images of Ni/CeO$_x$ (2 A). (f) XRD patterns and (g) Raman spectra of the designed films.

decreasing as the current density increases (Fig. S5 and S9–S12 and Note S1, ESI†). Among all films, Ni/CeO$_x$ (2 A) features the highest electrochemically active surface area (ECSA), as shown in Fig. S20 (ESI†), achieving a balance between the size and number of pores.

High-resolution TEM is employed to determine the chemical structure of Ni/CeO$_x$ (2 A). The analysis of d-spacing reveals a metallic Ni facet spaced at 2.03 Å interfacing with a CeO$_2$ facet with a spacing of 3.15 Å, matching those of the (111) facets of cubic Ni[36,37] (JCPDS card: 03-065-2865, and d-spacing (111) = 2.035 Å) and cubic CeO$_2$ (JCPDS card: 03-065-5923, and d-spacing (111) = 3.12 Å), respectively (Fig. 1e and Fig. S13a, ESI†). XRD confirms the chemical structure, where peaks at 2θ values of 44.55°, 51.86°, 76.39°, 92.97°, and 98.45° correspond to diffractions from the (111), (200), (220), (311), and (222) crystallographic planes of cubic Ni (JCPDS card: 03-065-2865), respectively (Fig. 1f). Another small peak is also observed at 28.55°, enclosed by a yellow box in Fig. 1f and zoomed in

Fig. S13i (ESI†). This peak corresponds to the (111) facet of cubic CeO$_2$[38,39] (JCPDS card: 03-065-5923) and appears small due to the low Ce content in the film, as reported earlier from ICP-OES and EDS data, in addition to the presence of amorphous regions, Fig. S13b (ESI†). The absence of this peak in the XRD pattern of the Ni film, alongside its appearance in the CeO$_x$ pattern, reaffirms the formation of the Ni/CeO$_x$ interface (Fig. S13i, ESI†). The patterns of the Ni film and all Ni/CeO$_x$ films show the characteristic peaks of cubic metallic Ni, while it is absent for the CeO$_x$ film (Fig. 1f and Fig. S13c, ESI†). Slight shifts in the 2θ Bragg angles of cubic metallic Ni peaks are observed for all Ni/CeO$_x$ films compared to the Ni film, indicating slight variations in the lattice parameters upon formation of the Ni/CeO$_x$ interface, see Fig. S13d–h and Table S2 (ESI†).[40] In addition, in all Ni/CeO$_x$ films (Fig. S13j, ESI†), the peak corresponding to cubic CeO$_2$ is evident, except for Ni/CeO$_x$ (0.1 A), where the presence of that peak cannot be confirmed, likely due to the minimal percentage of Ce in this film as reported by ICP-OES.

6250 | *Energy Environ. Sci.*, 2025, **18**, 6248–6259

This journal is © The Royal Society of Chemistry 2025

Raman spectroscopy confirms the resulting chemical structure, with Ni/CeO$_x$ (2 A) showing two bands at 573 and 1065 cm^{-1}, corresponding to the defect-induced mode (D band) and the second-order longitudinal optical mode (2LO band), respectively, as reported for Ni/CeO$_2$.[41] Interestingly, the intensity of the F$_{2g}$ symmetry band at 452 cm^{-1}, associated with scattering from symmetric O anions around the cations in the CeO$_2$ structure, is minimal (Fig. 1g).[42] The intensity ratio of the D band to the F$_{2g}$ band ($I_D/I_{F_{2g}}$) indicates the amount of O vacancies present in CeO$_2$.[41,43,44] Accordingly, the resulting Ni/CeO$_x$ (2 A) film is highly defective and non-stoichiometric, and therefore labelled as CeO$_x$ instead of CeO$_2$, leading to the appearance of Ce^{3+} in addition to Ce^{4+}.[43] Raman spectra of the other deposited films (Fig. S14a, ESI†) show that the sequence of the ($I_D/I_{F_{2g}}$) ratio of these films is CeO$_x$ < Ni/CeO$_x$ (0.1 A) < Ni/CeO$_x$ (0.5 A) < Ni/CeO$_x$ (1 A) < Ni/CeO$_x$ (3 A) < Ni/CeO$_x$ (2 A). These data refer to structural differences between the designed films, where Ni/CeO$_x$ (2 A) exhibits the highest degree of defects.

The oxidation states of the constituent elements in Ni/CeO$_x$ (2 A) are investigated through top-surface and depth-profiling XPS analyses. Deconvolution of the Ni 2p spectrum at the top surface (Fig. 2a) indicates that Ni is mostly metallic (Ni^0) with the presence of Ni^{2+} and Ni^{3+} ions, likely resulting from the oxidation of the top atomic layers by atmospheric oxygen.[45,46] This is further supported by depth-profiling XPS, showing that the deeper the layer, the bigger the shift towards the metallic Ni peak (Fig. 2d). The 3d spectrum of Ce at the top surface (Fig. 2b) is deconvoluted into Ce^{3+} ions, which are related to the

formation of O vacancies,[47] and Ce^{4+} ions,[48,49] with the former appearing larger in quantity, supporting the formation of defective Ce oxides with multiple Ce oxidation states as deduced from Raman spectra (Fig. 1g). Inspection of depth-profiling XPS of Ce (Fig. 2e) reveals that these oxidation states coexist throughout the tested depth, with the intensity of Ce^{3+} and Ce^{4+} peaks getting closer as the depth increases. Supporting these observations, the deconvolution of the O 1s spectrum at the top surface (Fig. 2c) reveals the presence of oxides, adsorbed O, and hydroxides, where hydroxides and adsorbed O appear dominant, likely due to Ni oxidation by atmospheric air, bearing in mind the large atomic percentage of Ni, revealed by ICP-OES and SEM-EDS. Interestingly, substantial changes manifest in the O 1s spectra upon testing deeper layers of the catalyst layer (Fig. 2f). A clear shift towards the oxide peak and a diminution of the hydroxide and adsorbed O peaks are observed at deeper catalyst layers. This is explained by the presence of Ce oxides and the absence of Ni hydroxides. This shift affirms the presence of metallic Ni and Ce oxides at deeper layers and the formation of Ni/CeO$_x$ interfaces. On the other hand, top-surface XPS spectra (Fig. S14b and c, ESI†) of the CeO$_x$ (2 A) film show a higher Ce^{4+} content relative to Ce^{3+}, confirming a lower degree of O defects in CeO$_x$ (2 A) compared to Ni/CeO$_x$ (2 A),[47] consistent with Raman data (Fig. S14a, ESI†).

Electrocatalytic activity of Ni/CeO$_x$ heterostructures

The as-prepared Ni/CeO$_x$ (2 A) catalyst demonstrates superb HER activity in 1.0 M KOH (Fig. 3a–c), outperforming the benchmark Pt/C catalyst. It exhibits zero onset overpotential with a significantly high exchange current density (i_0) of 7 mA cm^{-2} (Fig. 3c), indicating remarkable intrinsic activity and fast charge transfer. Notably, it achieves a high current density of 1000 mA cm^{-2} at remarkably low overpotentials of 201 mV and 157 mV at 20 °C and 60 °C, respectively (Fig. S15a, ESI†). These values position the Ni/CeO$_x$ (2 A) catalyst as one of the best-performing catalysts reported in the literature for the ampere-level HER, comparable or even outperforming Pt-based catalysts (Table S3 and Fig. S16, ESI†).

Additionally, the Tafel slope was measured and found to be 41 mV dec^{-1}, referring to the Heyrovsky step as the rate-determining step (RDS) and indicating facilitated charge transfer over Ni/CeO$_x$ (2 A) (Fig. 3b).[16] This is further supported by impedance spectroscopy with the distribution of relaxation times (DRT) analysis,[50] which shows a single, small charge transfer resistance peak (p3, possibly corresponding to the Heyrovsky step), while p1 represents the ohmic resistance in the cell (Fig. 3d). On the other hand, the deposited CeO$_x$ film displays a larger Tafel slope of 97 mV dec^{-1} and a smaller i_0 value of 0.17 mA cm^{-2}, suggesting sluggish charge transfer. This value, falling between 120 and 40 mV dec^{-1}, implies a dual control of the HER rate by both Volmer and Heyrovsky steps.[16,51] This signifies a notable deceleration occurring at the Volmer step, attributed to the absence of interfaced Ni sites that would help polarise and dissociate water molecules and act as H adsorption sites. Therefore, two much larger charge transfer peaks (p2 and p3, possibly corresponding to Volmer
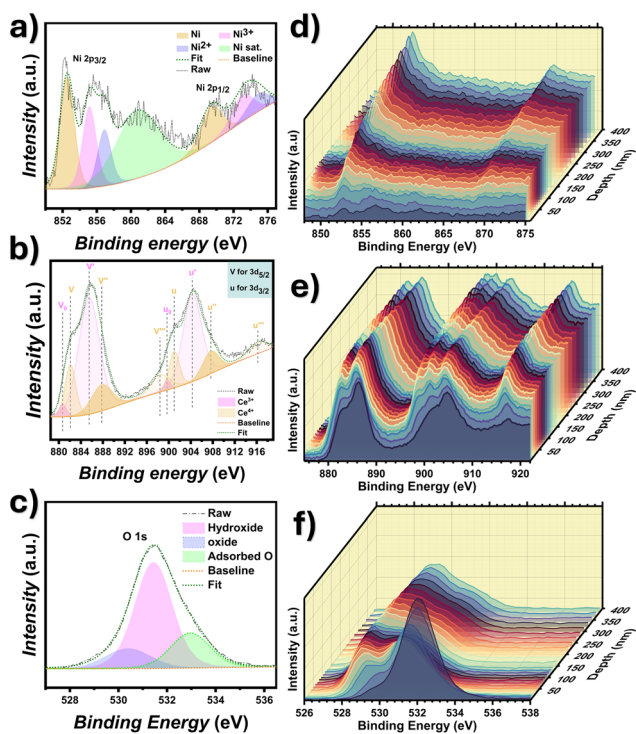

Fig. 2 XPS spectra of the Ni/CeO$_x$ (2 A) catalyst. Top-surface (a)–(c) and depth-profiling. (d)–(f) XPS spectra of the Ni/CeO$_x$ (2 A) film. Ni 2p spectra (a) and (d), Ce 3d spectra (b) and (e), and O 1s spectra (c) and (f).
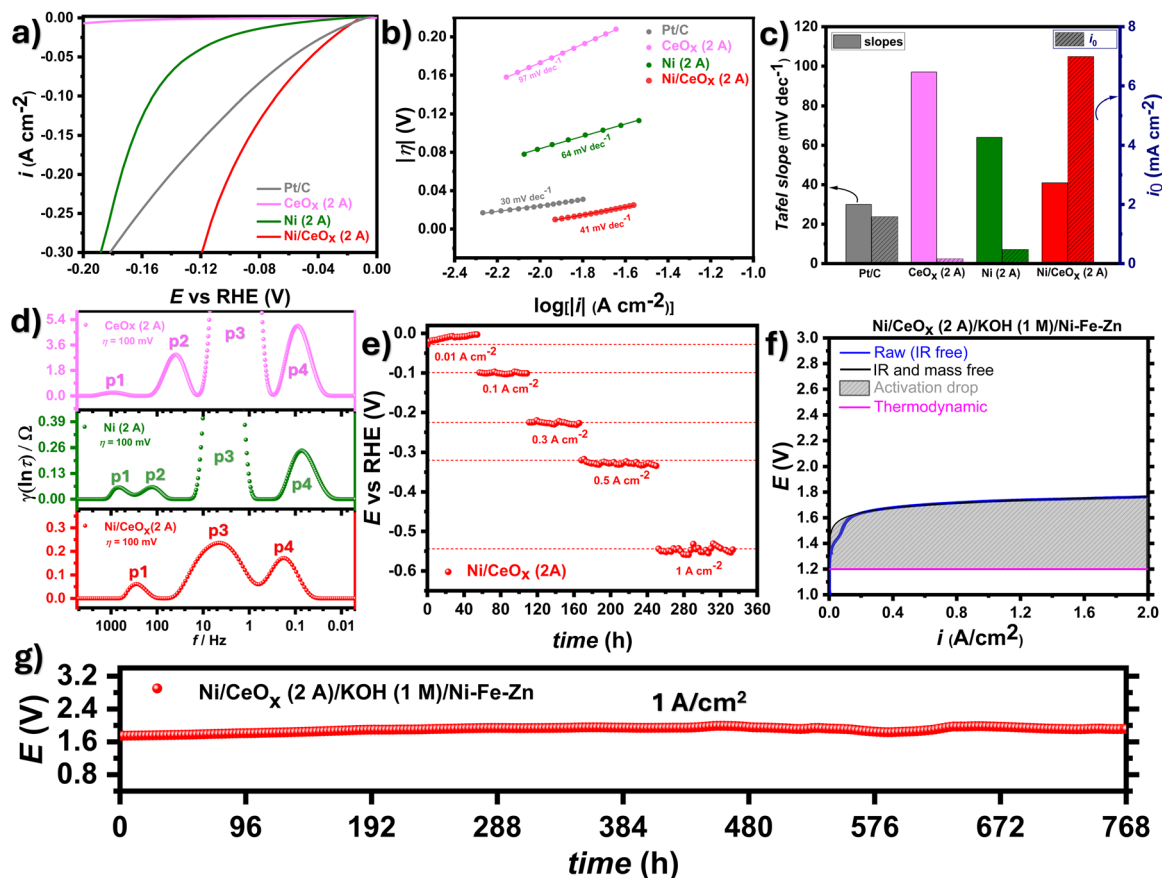
This journal is © The Royal Society of Chemistry 2025

Energy Environ. Sci., 2025, **18**, 6248–6259 | **6251**

Fig. 3 Electrocatalytic activity of the designed catalysts. (a) HER LSVs, (b) HER Tafel plots, (c) Tafel slopes and exchange current densities of the designed films. (d) DRT analysis for the HER at the designed films. (e) HER chronopotentiogram of Ni/CeO$_x$ (2 A) at 20 °C. (f) Deconvoluted LSV and (g) chronopotentiogram at 1 A cm^{-2} in a 2-electrode electrolysis cell at 60 °C.

and Heyrovsky steps, respectively) are observed in the DRT analysis. As a result, unobservable HER currents of 0.745 and 2.1 mA cm^{-2} are driven by overpotentials of 100 and 150 mV. As for the deposited Ni film, it shows a Tafel slope of 64 mV dec^{-1} and an i_0 value of 0.48 mA cm^{-2}, which fall between those of CeO$_x$ and Ni/CeO$_x$ (2 A), indicating moderate charge transfer kinetics with i_0 significantly lower than that of Ni/CeO$_x$ (2 A). Accordingly, p2 and p3 DRT peaks appear with the medium area, and overpotentials of 100 and 150 mV drive HER currents of 23.5 and 94.5 mA cm^{-2} at the Ni catalyst. Such an inferior activity in the absence of CeO$_x$ sites highlights again the crucial effect of Ni/CeO$_x$ interface formation, where CeO$_x$ sites help polarise and dissociate water molecules and provide desorption sites for the hydroxide byproduct.

As for the other Ni/CeO$_x$ catalysts deposited at different current densities, the observed activities in the low-current charge-transfer-controlled region follow this order: Ni/CeO$_x$ (0.1 A) < Ni/CeO$_x$ (0.5 A) < Ni/CeO$_x$ (1 A) < Ni/CeO$_x$ (3 A) < Ni/CeO$_x$ (2 A) (Fig. S15b, ESI†). This order is intriguingly the same as the degree of defects observed among these catalysts from Raman spectra. This observation suggests that the number of O vacancies acts as a descriptor for the charge transfer speed among metal/metal oxide interface catalysts: the more defective the catalyst is, the faster the charge transfer. In agreement, Tafel

slopes come in reverse order, approaching the theoretical value of the Volmer RDS as the degree of defects decreases (Fig. S17, ESI†). In conclusion, the higher HER activity of the Ni/CeO$_x$ (2 A) film, compared to other Ni/CeO$_x$ films in the low-current region, can be attributed to the highest degree of defects in this film, which eases the charge transfer and water polarisation and dissociation processes.

For the concentration overpotential, Ni/CeO$_x$ (2 A) exhibits the fastest mass transfer with the smallest low-frequency DRT peak (p4), followed by Ni, whereas CeO$_x$ suffers from significant limitations (Fig. 3d). In high-current regions, the non-intrinsic contributions are substantial and correlate with the number of accessible active sites. Accordingly, the ECSA is measured for all deposited films (Fig. S18 and S19, ESI†), revealing that the CeO$_x$ film, as expected, has the lowest ECSA due to the absence of macropores, far lower than that of the macroporous Ni film (Fig. S20a, ESI†). Notably, Ni/CeO$_x$ (2 A) exhibits the highest ECSA, with 479 cm$^2_{ECSA}$ cm$^{-2}_{geo}$, a high surface area that signifies the non-intrinsic activity component and the accelerated mass transfer. Although all Ni/CeO$_x$ catalysts show higher ECSA values than Ni and CeO$_x$ films, the gravimetric-specific ECSA, which is more reflective of morphology, refers to a higher value for the macroporous Ni film over the non-porous Ni/CeO$_x$ films, as expected.

6252 | Energy Environ. Sci., 2025, 18, 6248–6259

This journal is © The Royal Society of Chemistry 2025

The gravimetric-specific ECSA of Ni is still inferior to other macroporous Ni/CeO$_x$ films, where Ni/CeO$_x$ (2 A) keeps exhibiting the highest value (Fig. S20b, ESI†). To reaffirm the intrinsic activity component of Ni/CeO$_x$ (2 A), all LSVs are normalised to ECSA values in Fig. S20c (ESI†), where Ni/CeO$_x$ (2 A) remains the best-performing catalyst intrinsically. Turnover frequency (TOF) measurements are also conducted to confirm the superiority of the Ni/CeO$_x$ (2 A) catalyst, both intrinsically and non-intrinsically (Fig. S21, ESI†). The Ni/CeO$_x$ (2 A) catalyst has the highest number of active sites owing to its special balanced macro/mesoporous structure, reflecting enhanced mass transfer and non-intrinsic catalysis superiority. Additionally, after normalising the measured LSVs to obtain the corresponding TOFs, the Ni/CeO$_x$ (2 A) catalyst still exhibits the highest TOF, referring to the highest intrinsic activity among the deposited catalysts.

The durability of the Ni/CeO$_x$ (2 A) catalyst is evaluated at multiple current densities of up to 1 A cm^{-2} for 2 weeks (Fig. 3e). The Ni/CeO$_x$ film shows great stability even at high current densities like 1 A cm^{-2}, where no decay is noticed, reflecting the ability of the designed interface and macro/mesoporosity to survive under such harsh conditions. Furthermore, post-stability characterization studies (Fig. S22, ESI†) reveal that Ni/CeO$_x$ (2 A) maintains its elemental composition, morphology (including the cauliflower-like particles and the macro/mesoporosity), and structure. Nitrogen adsorption BET isotherm data (Fig. S22, ESI†) show nearly the same average mesopore diameter (7.1 nm) and the same type IV(b)[52] isotherm with a continuous absence of hysteresis, suggesting continued efficient gas desorption. Reconstruction of the CeO$_x$ sites into more ordered crystals is observed during the HER, yielding sharper CeO$_2$ diffraction peaks (Fig. S22g, ESI†). These observations affirm the stability of the designed heterostructured catalyst for practical ampere-level applications.

The performance of Ni/CeO$_x$ (2 A) is evaluated for full water electrolysis by coupling with an active OER (Ni–Fe–Zn) catalyst (Fig. S23 and S24 and Note S2, ESI†). In a 2-electrode alkaline electrolysis cell, 500, 1000, and 2000 mA cm^{-2} are achieved at 60 °C at cell voltages of 1.689, 1.73, and 1.764 V, corresponding to overall cell overpotentials of 489, 530, and 561 mV, respectively (Fig. 3f). Following the overpotential deconvolution procedure outlined in the calculation methods section (ESI†), these overpotentials are found to be mostly activation overpotentials rather than concentration overpotentials. This indicates the efficient mass transfer properties of the catalyst at high current densities. The electrolysis cell exhibits excellent stability for 768 h at 1 A cm^{-2} (Fig. 3g).

The Ni/CeO$_x$ catalyst is further applied for the AEMWE. When the HER and OER catalysts are assembled with a PiperION-20 membrane, current densities of 5, 4, and 3 A cm^{-2} are achieved at cell voltages of 2.078, 2.001, and 1.918 V at 60 °C, with IR-free overpotentials of 594, 573, and 547 mV, respectively (Fig. 4b), placing the designed catalysts and AEMWEs among the best reported in the literature (Table S4, ESI†). The designed AEMWE produces hydrogen at a high electrical efficiency of 42.0 kW h kg^{-1}, when operating at 0.25 A cm^{-2} (Fig. 4d). Therefore, the cost of hydrogen production is $0.84 per kg when the electricity cost is $0.02 per kW h,[53] meeting the 2030 price target ($1 per kg) of the U.S. Department of Energy (DOE).[54] This corresponds to energy efficiencies of 95% and 80%, based on the higher (HHV) and lower (LHV) heating values of hydrogen, respectively (Fig. 4d). Accordingly, the AEMWE device surpasses the International Renewable Energy Agency (IRENA) energy efficiency (LHV) target for 2050 (>75%) when operating at current densities below 0.66 A cm^{-2}.[5] On the other hand, with the X37-50 membrane, voltages of 1.754, 1.843, and 1.981 V drive lower current densities of 0.5, 1, and 2 A cm^{-2}, respectively, due to the higher ohmic resistance of the X37-50 membrane (Fig. 4c). Notably, the observed IR-free overpotentials are 503, 542, and 579, respectively, approximately matching those 489, 530, and 561 mV values observed at the IR-free polarization curve at the 2-electrode alkaline electrolysis cell. Accordingly, IR-free testing in 2-electrode alkaline electrolysis cells can sometimes predict the observed overpotentials in AEMWEs free from *IR* drops. The deconvolution of the observed overpotentials in both AEMWEs shows a similar behaviour to that observed in the 2-electrode cell, with nearly no noticeable concentration overpotentials. This points to the unique macro/mesoporous morphology attained by the DHBT method. The presence of various pore sizes increases the accessible surface area, accommodates different bubble sizes, prevents site blockage, and facilitates electrolyte and bubble (mass) transfer. Reduced activation overpotentials refer to the tailored structures of the designed catalysts to accelerate the charge transfer processes. AEMWE durability is evaluated *via* chronopotentiometry by applying 0.5 A cm^{-2} for 96 h. No voltage decay is observed throughout the testing duration, referring to materials' stability at the operating current and conditions (Fig. 4e). The faradaic efficiency of hydrogen production is measured by gas chromatography (GC) at 0.5 A cm^{-2}, reaching 99.98% (Fig. S25, ESI†).

Theoretical mechanistic analysis

The origin of the superior intrinsic activity of Ni/CeO$_x$ catalysts towards the HER is revealed using DFT calculations. The lattice parameters of Ni, CeO$_2$, and Ni/CeO$_2$ structures used in calculations are provided in Table S5 (ESI†). Additionally, to investigate the impact of O vacancies on HER electrocatalysis, three defective structures (CeO$_{2-\delta}$, Ni/CeO$_{2-\delta}$, and Ni/CeO$_{2-2\delta}$) are constructed by selecting the most stable vacancy position (Fig. S28–S30, ESI†). In alkaline solutions, the HER proceeds *via* water adsorption onto the catalyst surface, followed by dissociation into H$^+$ and OH$^-$ ions. The H$^+$ ions then gain electrons and become ready for combination to desorb and evolve hydrogen gas *via* either Tafel or Heyrovsky steps, while the OH$^-$ ions desorb into the solution.[16,29] HER elementary steps at Ni, CeO$_{2-\delta}$, Ni/CeO$_{2-\delta}$, and Ni/CeO$_{2-2\delta}$ catalysts are investigated and illustrated in Fig. S31–S34 (ESI†).

The Gibbs free energy of hydrogen adsorption (ΔG_H) is a main descriptor for the intrinsic activity of catalysts towards the HER. A value proximal to zero indicates superior HER performance, where a balance between H adsorption and desorption is achieved, neither excessively strong nor too weak.[55] As shown

This journal is © The Royal Society of Chemistry 2025

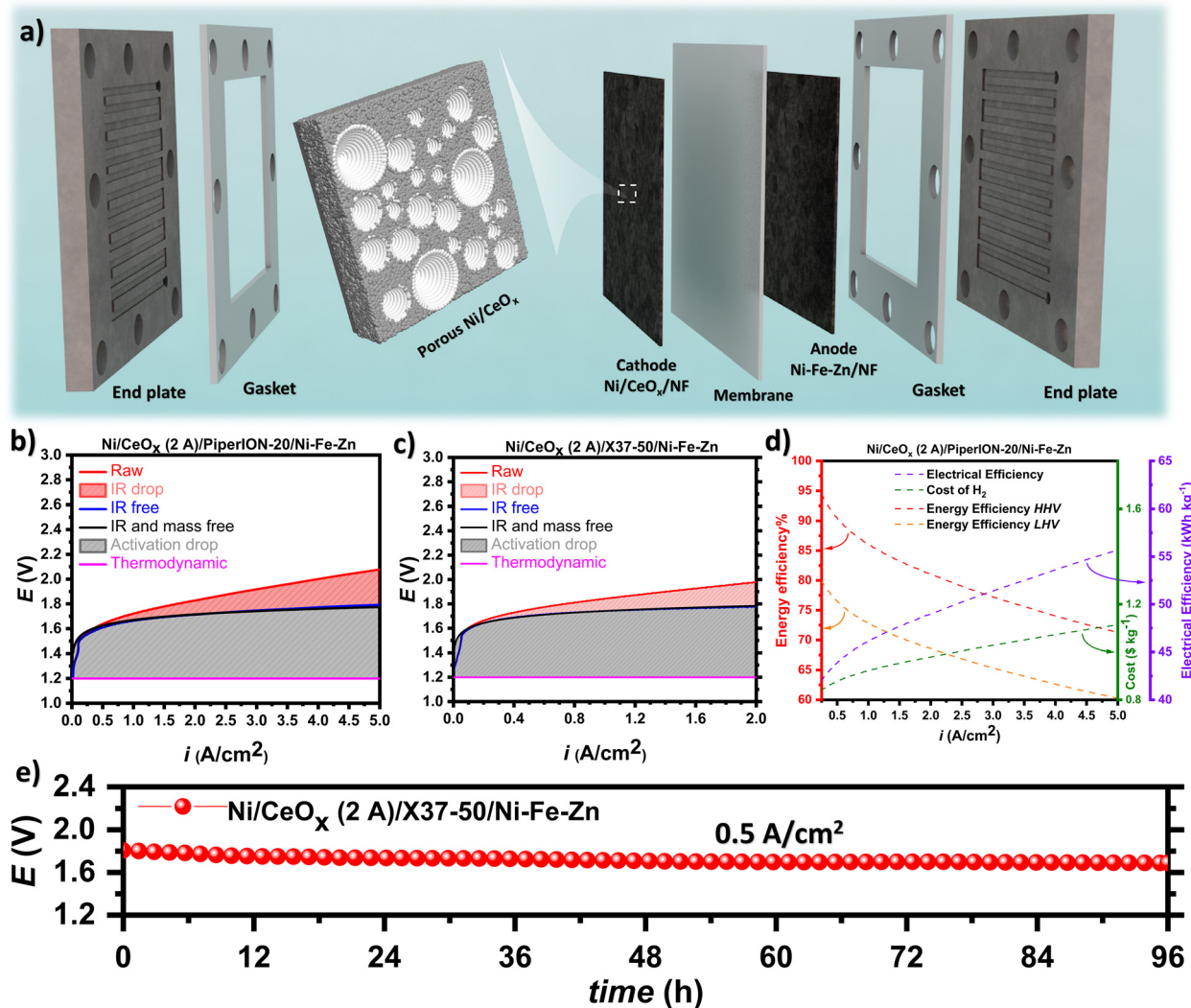*Energy Environ. Sci.*, 2025, **18**, 6248–6259 | **6253**

Fig. 4 AEMWE measurements. (a) Schematic diagram of an AEMWE. Deconvoluted LSV at 60 °C for (b) AEMWE with PiperION-20 and (c) AEMWE with X37-50. (d) Energy and electrical efficiencies of AEMWE with PiperION-20 at 60 °C. (e) Chronopotentiogram at 0.5 A cm^{-2} for the AEMWE with X37-50 at 60 °C.

in Fig. 5a, ΔG_H values follow a near-zero-based sequence, Ni/CeO$_{2-2\delta}$ (0.22 eV) > Ni/CeO$_{2-\delta}$ (0.31 eV) > Ni (0.48 eV) > CeO$_{2-\delta}$ (−0.54 eV), mirroring the electrocatalytic sequence towards the HER. This supports the synergistic impact of forming Ni/CeO$_x$ interfaces compared to individual Ni or CeO$_x$ on boosting HER activity by tuning hydrogen adsorption energies. Meanwhile, it highlights the effect of O vacancy concentration on modulating the catalyst's adsorption capacity for hydrogen, wherein more defects at the interface enhance hydrogen adsorption/desorption energetics.

Water dissociation proceeds through three stages: the initial state (IS), which involves water adsorption, followed by a transition state (TS) of bond disruption, leading to complete dissociation into adsorbed H and OH$^-$ in the final state (FS). During these processes, three other Gibbs free energy values are crucial besides ΔG_H due to the lack of protons in alkaline media.[56] These values are G_{IS} (free energy of water adsorption), ΔG_{TS-IS} (a kinetic parameter referred to as a water dissociation

energy barrier), and ΔG_{FS-IS} (a thermodynamic parameter referring to the spontaneity of the dissociation process). The lower these values, the more favourable water dissociation in thermodynamic and kinetic aspects. As illustrated in Fig. 5b, Fig. S35 (ESI†), and Table S6 (ESI†), Ni/CeO$_x$ interfaces exhibit rapid (small kinetic energy barriers, ΔG_{TS-IS}) and spontaneous water dissociation (negative ΔG_{FS-IS} values). On the other hand, although CeO$_{2-\delta}$, demonstrates the best water adsorption energy (0.21 eV), it exhibits non-spontaneous (positive ΔG_{FS-IS} value of 0.24 eV) water dissociation with sluggish kinetics and a large energy uphill of 1.36 eV. Separate Ni exhibits the worst water adsorption energy (0.68 eV) along with the largest dissociation energy barrier (1.47 eV). However, it outperforms separate CeO$_x$ due to the lower non-spontaneity barrier (ΔG_{FS-IS}) and more optimal hydrogen adsorption energy (ΔG_H). For Ni/CeO$_x$ interfaces, water adsorption and dissociation processes over Ni/CeO$_{2-2\delta}$ are more thermodynamically and kinetically favoured than over Ni/CeO$_{2-\delta}$, reflecting the optimisation impact of the
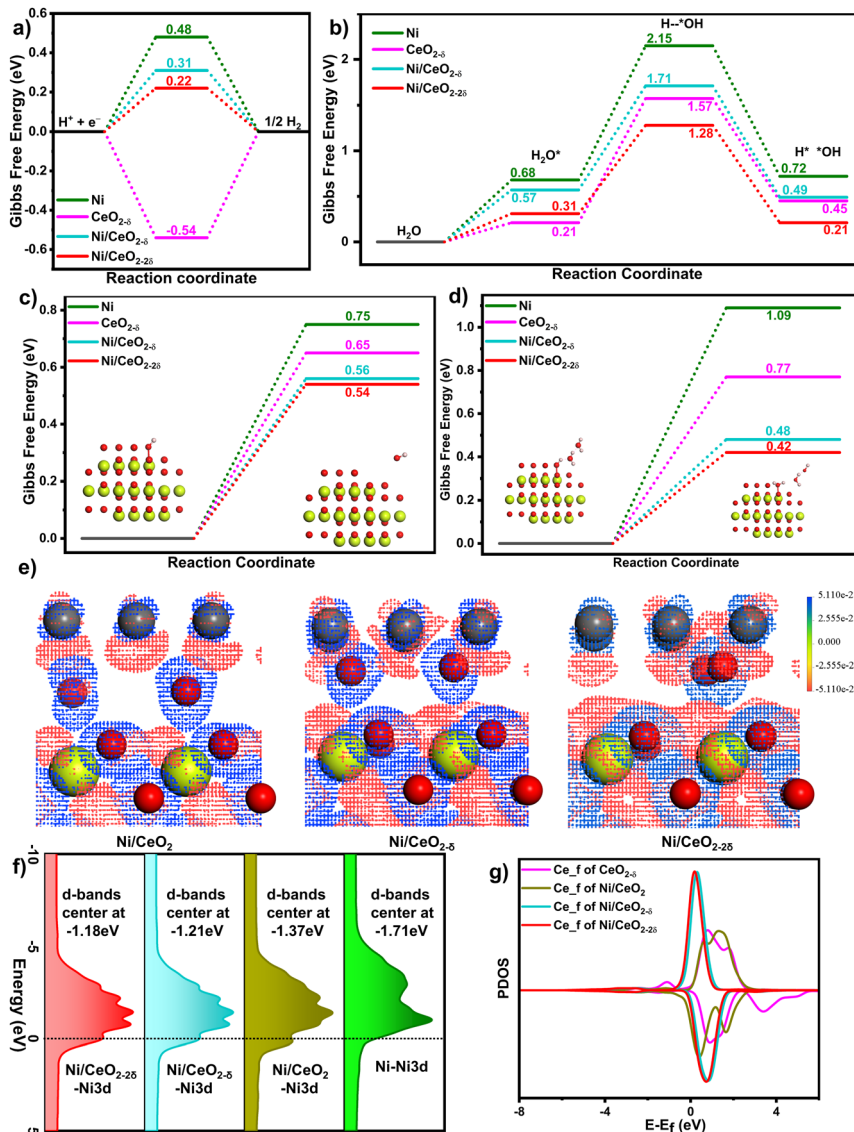
6254 | *Energy Environ. Sci.*, 2025, **18**, 6248–6259

This journal is © The Royal Society of Chemistry 2025

Fig. 5 Theoretical calculations. Gibbs free energy of HER processes in alkaline media over Ni, $CeO_{2-\delta}$, $Ni/CeO_{2-\delta}$, and $Ni/CeO_{2-2\delta}$ catalysts: (a) hydrogen adsorption process. (b) Water adsorption and dissociation processes. (c) OH* direct desorption process. (d) Water-assisted OH^- indirect desorption process. (e) Electron density difference images at the interface of Ni/CeO_2 $Ni/CeO_{2-\delta}$, and $Ni/CeO_{2-2\delta}$ (blue represents electron rich and red represents electron deficient). (f) Partial density of states (PDOS) of Ni, Ni/CeO_2, $Ni/CeO_{2-\delta}$, and $Ni/CeO_{2-2\delta}$ (Ni 3d orbits). (g) Partial density of states (PDOS) of $CeO_{2-\delta}$, Ni/CeO_2, $Ni/CeO_{2-\delta}$, and $Ni/CeO_{2-2\delta}$ (Ce 4f orbits). Atoms colors: Ni: grey, Ce: lime green, O: red, and H: light pink (Table S7, ESI†).

structure defects on these processes besides the hydrogen adsorption process. These observations suggest that at Ni/CeO_x interfaces, water adsorption occurs at O vacancies and then disruption of water bonds occurs when hydrogen is pulled towards interfaced Ni, leading to complete water dissociation and leaving dissociated H adsorbed at Ni, while dissociated hydroxide adsorbed at the O vacancy.

The differential charge densities of Ni/CeO_2, $Ni/CeO_{2-\delta}$, and $Ni/CeO_{2-2\delta}$ are calculated to confirm the proposed role of O vacancies in the HER (Fig. 5e). At the interface of Ni/CeO_2, electrons are concentrated around the O atom, resulting in electron enrichment at the interface. This enrichment is advantageous for attracting water H but not for OH, leading to relative deceleration in water adsorption and dissociation.

As the concentration of O vacancies increases, a red cloud (indicative of electron deficiency) is observed at the O vacancy site, signifying a localized positive charge in this region, which is beneficial for attracting OH. Meanwhile, electron enrichment occurs around Ni, facilitating the attraction of H. This preferential attraction of OH and H at the O vacancy and Ni sites, respectively, disrupts water bonds and promotes water dissociation, thereby leading to Heyrovsky-controlled kinetics, diverging from the sluggish Volmer RDS as depicted in Fig. 3b.

To verify this concept, the PDOSs of the Ni 3d orbits of Ni, Ni/CeO_2, $Ni/CeO_{2-\delta}$, and $Ni/CeO_{2-2\delta}$ are calculated (Fig. 5f). The upshift of the d-band centre of Ni/CeO_2 compared to Ni indicates a synergistic effect between CeO_2 and Ni, with electrons at higher energy levels facilitating H adsorption.[57,58]

As the concentration of vacancies increases, the d-band centre shifts further upward, indicating that O vacancies can enhance the H adsorption capacity of Ni sites. Similarly, compared to $CeO_{2-\delta}$ and Ni/CeO_2, $Ni/CeO_{2-\delta}$, and $Ni/CeO_{2-2\delta}$ have more bonding orbitals below the Fermi level and fewer antibonding orbitals above the Fermi level (Fig. 5g). Bonding orbitals signify stable bonding in the structure, indicating that O vacancy-rich CeO_2 forms a stable interface with Ni.

Hydroxide desorption is a crucial process for the retrieval of active sites through two possible pathways: either direct desorption to the aqueous phase or indirect release from the aqueous phase through a water-assisted proton exchange pathway.[59] The latter can accelerate the HER in alkaline media by skipping the water adsorption step. The calculation results (Fig. 5c and d) show that Ni and $CeO_{2-\delta}$ prefer the direct hydroxide desorption pathway, while for Ni/CeO_x interfaces, the water-assisted hydroxide desorption pathway is preferred, leading to accelerated kinetics. $Ni/CeO_{2-2\delta}$ shows the lowest energy barrier for hydroxide desorption, implying the acceleration impact with a higher degree of defects. Based on this discussion and the high conductivity observed from the DOS plots (Fig. S36, ESI†), the intrinsic activity of the Ni/CeO_x (2 A) catalyst, with lowered activation overpotential, can be explained.

Conclusions

A Ni/CeO_x interface is tailored by tuning the deposition current density and applied for efficient and robust hydrogen evolution in alkaline media and AEMWEs. Accelerated charge transfer is observed for the Ni/CeO_x film compared to Ni and CeO_x films, attributed to synergistic effects at the defective interface. This synergy facilitates water dissociation, hydroxide desorption and H adsorption processes, as evidenced by theoretical calculations. Concentration overpotentials are also mitigated due to the hierarchical pores generated, which provide suitable channels for electrolyte and bubble (mass) transfer. These findings pave the way for further research to investigate the impacts of oxygen vacancies and porosity on the HER mechanism. In the AEMWE, the overall concentration and an activation overpotential of 594 mV enable hydrogen production at 5 A cm^{-2}. The designed AEMWE surpasses the IRENA voltage efficiency (LHV) target for 2050 ($>75\%$) at a current density below 0.66 A cm^{-2}.[5] The method used in this study to deconvolute the sources of overpotentials is recommended to predict AEMWE performance from two-electrode cell tests and to decouple limitations, allowing for more targeted solutions for the identified overpotentials.

Experimental

Materials

Cerium nitrate hexahydrate $Ce(NO_3)_3\cdot6H_2O$, iron sulphate heptahydrate $FeSO_4\cdot7H_2O$, and zinc nitrate hexahydrate $ZnSO_4\cdot6H_2O$ were purchased from Sigma-Aldrich. Nickel sulphate hexahydrate $NiSO_4\cdot6H_2O$, ammonium sulphate $(NH_4)_2SO_4$, ammonium chloride NH_4Cl, and potassium hydroxide KOH were purchased from Chem-Supply Australia. Trisodium citrate dihydrate $Na_3C_6H_5O_7\cdot2H_2O$ was purchased from Merck. The Sustainion X37-50 membrane and the XA-9 ionomer were purchased from Dioxide Materials. The PiperION-20 membrane, PiperION ionomer, Pt/C (20% platinum on Vulcan XC-72R, carbon), and PFSA dispersion (D5, 5%) were purchased from the FUELCeLL store. All chemicals were used as received without further purification.

Catalyst synthesis

Synthesis of Ni/CeO_x films. A deposition bath, comprising 0.027 M $NiSO_4$, 0.003 M $Ce(NO_3)_3$, and 0.600 mM $(NH_4)_2SO_4$ in Milli-Q water, was prepared by dissolving $NiSO_4$ and $Ce(NO_3)_3$ together, while $(NH_4)_2SO_4$ was dissolved separately before mixing with the other two dissolved chemicals to form the specified concentrations. Dissolution kinetics were significantly impeded if all chemicals were mixed in solid form before dissolution. A two-electrode cell was utilised for deposition, with a 9 cm^2 graphite plate (3 mm thickness) as the anode and a 1 cm^2 pressed (3000 psi) Ni foam (1 mm thickness) as the cathode and deposition substrate. Ni foam was pressed to flatten its sharp tips, which sometimes led to membrane penetration and short circuits in AEMWEs if used as received without pressing. Additionally, the same deposition conditions were applied to a 1 cm^2 Al foil (0.3 mm thickness) that replaced Ni foam and served as another cathodic substrate for catalyst growth. Various current densities (0.1, 0.5, 1, 2, and 3 A cm^{-2}) were applied for different durations (150, 30, 15, 7.5, and 5 min, respectively) to deposit the targeted catalysts, allowing the same charge to pass.

Synthesis of Ni and CeO_x films. A Ni film was deposited from a solution containing 0.030 M $NiSO_4$ and 0.600 mM $(NH_4)_2SO_4$. The deposition process followed the same dissolution and mixing sequence, as well as the same cell configuration for Ni/CeO_x preparation but 2 A cm^{-2}, for 7.5 min, was the only applied current density. The CeO_x film was deposited under conditions identical to those of the Ni film and the only variation was the replacement of $NiSO_4$ with $Ce(NO_3)_3$, maintaining the same concentration of 0.030 M.

Synthesis of the Pt/C film. A uniform ink made from 5 mg of commercial Pt/C mixed with 475 μL of deionized water, 500 μL of ethanol, and 25 μL of 5% PFSA dispersion binder was drop-cast onto a 1 cm^2 carbon fibre paper substrate (AvCarb® MGL190).

Synthesis of the Ni–Fe–Zn film. The Ni–Fe–Zn film was prepared from a deposition bath that comprised 0.050 M $NiSO_4$, 0.050 M $FeSO_4$, 0.050 M $ZnSO_4$, 0.200 M trisodium citrate $Na_3C_6H_5O_7$, and 1.0 M NH_4Cl in Milli-Q water. All salts were dissolved together directly in one pot. The same deposition cell configuration was employed, and a current density of 2 A cm^{-2} was applied for 7.5 min.

Characterization techniques

Scanning electron microscopy (SEM) micrographs for the catalysts over pressed Ni foam or Al foil were captured using a JEOL 7001F Schottky field emission microscope connected with an

6256 | *Energy Environ. Sci.*, 2025, **18**, 6248–6259

This journal is © The Royal Society of Chemistry 2025

energy-dispersive X-ray spectroscopy (EDS) detector to determine the elemental composition and distribution. Both high-resolution transmission electron microscopy (HRTEM) and scanning transmission electron microscopy (STEM) were conducted using a JEOL JEM-F200 multi-purpose electron microscope operating at 200 kV, where powdery catalyst samples were peeled off by ultrasonication in ethanol and loaded on a copper grid for testing. Surface area characteristics, including pore sizes and volumes, were measured *via* Brunauer–Emmett–Teller (BET) analysis conducted using a TriStar II Plus instrument for a powdery sample peeled off by scratching. X-ray powder diffraction (XRD) was carried out using a Malvern PANalytical Aeris diffractometer with Cu-Kα radiation for powdery catalysts loaded on zero-background holders. Raman spectra were recorded using a Renishaw inVia Qontor microscope with a laser excitation wavelength of 514 nm. The amounts of Ni and Ce in the samples were determined using inductively coupled plasma optical emission spectroscopy (ICP-OES, Optima7000). X-ray photoelectron spectroscopy (XPS) results were obtained using a Thermo ESCALAB250i spectrometer, and all binding energies in the XPS spectra were calibrated for specimen charging by referencing C 1s to 284.8 eV. Depth-profiling XPS was performed using a Thermo ESCALAB250i spectrometer by applying an Ar ion beam at 1 keV at an etching rate of 0.18 nm s^{-1}.

Electrochemical measurements. All measurements were carried out using a CHI760E potentiostat. For high currents, a linked current booster was employed.

Half-cell reaction measurements. Linear sweep voltammetry (LSV) measurements, *IR* compensated, were carried out in 1.0 M KOH at a scan rate of 10 mV s^{-1} to test both the HER and the oxygen evolution reaction (OER). Tafel plots were created from LSV measurements, *IR* compensated, in 1.0 M KOH at a scan rate of 1 mV s^{-1}. Electrochemical impedance spectroscopy (EIS) measurements were performed at an overpotential of 100 mV for all films, with an amplitude of 5 mV in the frequency range of 10^5 to 0.01 Hz and after a steady state current was reached. The distribution of relaxation times (DRT) analysis of EIS was performed using the open MATLAB code provided by Ciucci's lab,[60] discarding the inductive data and using a second-order regularization derivative. Chronopotentiometry measurements were conducted in 1.0 M KOH at different current densities without *IR* compensation. The electrochemically active surface area (ECSA) was measured *via* cyclic voltammetry (CV), *IR* compensated, in a capacitive potential window at different scan rates. Turnover frequency (TOF) measurements were conducted *via* CV, IR compensated, within redox potential windows at a scan rate of 5 mV s^{-1} for all films except CeO$_x$, where 50 mV s^{-1} was employed to show observable currents. All measurements were carried out at 20 ± 2 °C except for one LSV measurement at 60 °C to test the best-performing HER catalyst at the operational temperature of the AEMWE.

Full-cell measurements. LSV for the full cell, *IR* compensated, was conducted in 1.0 M KOH at a scan rate of 10 mV s^{-1}. Similarly, a Tafel plot was generated from LSV measurements, *IR* compensated, in 1.0 M KOH at a scan rate of 1 mV s^{-1}.

A chronopotentiometry measurement, *IR* compensated, was carried out in 1.0 M KOH at 1 A cm^{-2}. These tests were carried out in a two-electrode electrolysis cell at 60 °C only, where Ni/CeO$_x$ (2 A) is the cathode catalyst and Ni–Fe–Zn is the anode catalyst.

AEMWE measurements. Using the catalyst-coated substrate (CSS) membrane-electrode assembly (MEA) technique, Ni/CeO$_x$ and Ni–Fe–Zn catalysts were assembled with either the PiPerION-20 membrane or the Sustainion (X37-50) membrane. A 1.0 M KOH solution was circulated from both sides of the electrolyser using two peristaltic pumps (SHENCHEN, LabS3) at 38 mL min^{-1} and 19 mL min^{-1} for the cathode and anode sides, respectively, considering the doubled rate of hydrogen gas evolution compared to oxygen. LSV measurements were conducted at a scan rate of 10 mV s^{-1} with no *IR* compensation, while Tafel plots are generated from IR-compensated LSVs obtained at a scan rate of 1 mV s^{-1}. Chronopotentiometry measurement, without *IR* compensation, was carried out using an X37-50-separated electrolyser by applying 0.5 A cm^{-2}. XA-9 or PiperION ionomers (both 5% in ethanol) were used to compare the activities of the AEMWEs in the absence and presence of ionomers. Three AEMWE configurations were designed, where 20 μL of XA-9 or PiperION ionomers were drop-cast on both the cathodic and anodic catalysts, 10 μL on each side, and left to dry before assembly to construct the first AEMWE. In the second configuration, 10 μL of XA-9 or PiperION ionomers were drop-cast solely on the anodic side, while the third configuration is ionomer-free. The XA-9 ionomer was exclusively utilised when the X37-50 membrane is employed, and similarly, the PiperION ionomer was used with the PiperION-20 membrane. All these tests were carried out at 60 °C only.

Theoretical computations

Calculations were conducted using the Materials Studio CASTEP module, employing density functional theory (DFT). The Perdew–Burke–Ernzserhof (PBE) exchange–correlation functional was employed under the generalized gradient approximation scheme, with a cut-off energy of 500 eV. All structural optimizations were performed with the force exerted on the atoms lower than 0.02 eV Å^{-1}, and the total energy convergence was set to 5.0 × 10^{-7} eV per atom.

During the structural optimization process, a 4 × 4 × 1 grid was utilised to sample CeO$_2$, Ni/CeO$_2$, CeO$_{2-\delta}$, Ni/CeO$_{2-\delta}$, and Ni/CeO$_{2-2\delta}$. The CeO$_{2-\delta}$ structure was generated by introducing defects onto the CeO$_2$ (111) surface, whereas Ni/CeO$_{2-\delta}$ and Ni/CeO$_{2-2\delta}$ involved defects created within the oxygen atomic layer at the Ni/CeO$_2$ heterojunction interface. To maximize the exposure of the active oxygen vacancy sites, the surface adsorption configuration of Ni/CeO$_{2-\delta}$ was selected in the (100) direction, while Ni/CeO$_{2-2\delta}$ was cut on the (010) plane.

For the calculation of the chemical formation energy of defects, taking CeO$_{2-\delta}$ as an example, the equation used is:

$$\Delta E_{\text{formation}} = E_{\text{CeO}_2} - E_{\text{CeO}_{2-\delta}} - \frac{1}{2}E_{\text{O}_2} \quad (1)$$

The Gibbs free energy of hydrogen adsorption (ΔG_{H}), which is a key parameter for determining the HER activity as proposed

This journal is © The Royal Society of Chemistry 2025

Energy Environ. Sci., 2025, **18**, 6248–6259 | **6257**

by Norskov et al.,[61] was calculated following the equations below:

$$\Delta E_{\text{H}} = E_{\text{ads}} - \frac{1}{2}E_{\text{H}_2} - E_{\text{Layer}} \quad (2)$$

$$\Delta G_{\text{H}} = \Delta E_{\text{H}} - \Delta\text{ZPE} - T\Delta S_{\text{H}} \quad (3)$$

where ΔE_{H} represents the H adsorption energy, E_{ads} denotes the total energy of H adsorption on the surface of catalysts, and E_{H_2} and E_{Layer} are the energies of the hydrogen molecule and the heterostructure, respectively. ΔZPE and ΔS_{H} are the zero-point energy and the entropy change of H adsorption, respectively. The value of $\Delta\text{ZPE} - T\Delta S_{\text{H}}$ was set as 0.24 eV. The water dissociation process and the dissociation energy barrier were computed by searching for the transition states using PBE.

Author contributions

I. O. B. conceived the idea, designed and carried out the experiments, collected data, and wrote the first draft of the manuscript, H. H. performed the DFT calculations and co-wrote, with I. O. B., the DFT part. Y. X. contributed to the electrochemical experimentation. S. W. revised the DFT part and performed the top-surface XPS measurements. Y. N. performed the TEM measurements. C. J. performed the Raman measurements. K. D. discussed the progress of the study. C. Z. supervised the project. All authors discussed the results and contributed to the writting of the manuscript.

Data availability

The data supporting this article have been included as part of the ESI.†

Conflicts of interest

There are no conflicts to declare.

Acknowledgements

References

1 M. R. Kraglund, M. Carmo, G. Schiller, S. A. Ansar, D. Aili, E. Christensen and J. O. Jensen, *Energy Environ. Sci.*, 2019, **12**, 3313–3318.

2 D. Li, E. J. Park, W. Zhu, Q. Shi, Y. Zhou, H. Tian, Y. Lin, A. Serov, B. Zulevi and E. D. Baca, *Nat. Energy*, 2020, **5**, 378–385.

3 M. J. Jang, S. H. Yang, M. G. Park, J. Jeong, M. S. Cha, S.-H. Shin, K. H. Lee, Z. Bai, Z. Chen and J. Y. Lee, *ACS Energy Lett.*, 2022, **7**, 2576–2583.

4 Q. Xu, L. Zhang, J. Zhang, J. Wang, Y. Hu, H. Jiang and C. Li, *EnergyChem*, 2022, 100087.

5 I. R. E. Agency, *Report*.

6 N. Du, C. Roy, R. Peach, M. Turnbull, S. Thiele and C. Bock, *Chem. Rev.*, 2022, **122**, 11830–11895.

7 S. Petrovic, *Electrochemistry Crash Course for Engineers*, Springer, 2021.

8 E. T. Ojong, J. T. H. Kwan, A. Nouri-Khorasani, A. Bonakdarpour, D. P. Wilkinson and T. Smolinka, *Int. J. Hydrogen Energy*, 2017, **42**, 25831–25847.

9 D. Liu, G. Xu, H. Yang, H. Wang and B. Y. Xia, *Adv. Funct. Mater.*, 2023, **33**, 2208358.

10 Y. Pan, J. Gao, E. Lv, T. Li, H. Xu, L. Sun, A. Nairan and Q. Zhang, *Adv. Funct. Mater.*, 2023, **33**, 2303833.

11 M. Wei, Y. Sun, J. Zhang, F. Ai, S. Xi and J. Wang, *Energy Environ. Sci.*, 2023, **16**, 4009–4019.

12 B. Wang, X. Zhu, X. Pei, W. Liu, Y. Leng, X. Yu, C. Wang, L. Hu, Q. Su and C. Wu, *J. Am. Chem. Soc.*, 2023, **145**, 13788–13795.

13 T. Zhao, S. Wang, C. Jia, C. Rong, Z. Su, K. Dastafkan, Q. Zhang and C. Zhao, *Small*, 2023, 2208076.

14 Y. Li, X. Tan, S. Chen, X. Bo, H. Ren, S. C. Smith and C. Zhao, *Angew. Chem., Int. Ed.*, 2019, **58**, 461–466.

15 Z. Chen, X. Li, J. Zhao, S. Zhang, J. Wang, H. Zhang, J. Zhang, Q. Dong, W. Zhang and W. Hu, *Angew. Chem., Int. Ed.*, 2023, **62**, e202308686.

16 G. Zhao, K. Rui, S. X. Dou and W. Sun, *Adv. Funct. Mater.*, 2018, **28**, 1803291.

17 K. Dastafkan, X. Shen, R. K. Hocking, Q. Meyer and C. Zhao, *Nat. Commun.*, 2023, **14**, 547.

18 Y. S. Park, J. Yang, J. Lee, M. J. Jang, J. Jeong, W.-S. Choi, Y. Kim, Y. Yin, M. H. Seo and Z. Chen, *Appl. Catal., B*, 2020, **278**, 119276.

19 L. Wan, Z. Xu, P. Wang, P.-F. Liu, Q. Xu and B. Wang, *Chem. Eng. J.*, 2022, **431**, 133942.

20 F. Razmjooei, T. Morawietz, E. Taghizadeh, E. Hadjixenophontos, L. Mues, M. Gerle, B. D. Wood, C. Harms, A. S. Gago and S. A. Ansar, *Joule*, 2021, **5**, 1776–1799.

21 J. Liu, G. Qian, T. Yu, J. Chen, C. Zhu, Y. Li, J. He, L. Luo and S. Yin, *Chem. Eng. J.*, 2022, **431**, 134247.

22 X. Yan, L. Tian, M. He and X. Chen, *Nano Lett.*, 2015, **15**, 6015–6021.

23 L. Peng, X. Zheng, L. Li, L. Zhang, N. Yang, K. Xiong, H. Chen, J. Li and Z. Wei, *Appl. Catal., B*, 2019, **245**, 122–129.

24 P. Patnaik, *Handbook of inorganic chemicals*, McGraw-Hill, New York, 2003, vol. 529.

25 Q. Qin, H. Jang, X. Jiang, L. Wang, X. Wang, M. G. Kim, S. Liu, X. Liu and J. Cho, *Angew. Chem.*, 2023, e202317622.

26 F. Jiang, S. Wang, B. Liu, J. Liu, L. Wang, Y. Xiao, Y. Xu and X. Liu, *ACS Catal.*, 2020, **10**, 11493–11509.

27 E. Sadeghi, S. Chamani, E. Erdem, N. S. Peighambardoust and U. Aydemir, *ACS Appl. Energy Mater.*, 2023, **6**, 7658–7671.

6258 | *Energy Environ. Sci.*, 2025, **18**, 6248–6259

This journal is © The Royal Society of Chemistry 2025

28 B. J. Plowman, L. A. Jones and S. K. Bhargava, *Chem. Commun.*, 2015, **51**, 4331–4346.

29 I. O. Baibars, M. G. Abd El-Moghny and M. S. El-Deab, *J. Environ. Chem. Eng.*, 2022, **10**, 108736.

30 B. Huang, X. Wang, W. Li, W. Tian, L. Luo, X. Sun, G. Wang, L. Zhuang and L. Xiao, *Angew. Chem., Int. Ed.*, 2023, e202304230.

31 C. González-Buch, I. Herraiz-Cardona, E. Ortega, J. García-Antón and V. Pérez-Herranz, *Int. J. Hydrogen Energy*, 2013, **38**, 10157–10169.

32 C. A. Marozzi and A. C. Chialvo, *Electrochim. Acta*, 2000, **45**, 2111–2120.

33 A. J. Aldykiewicz, A. J. Davenport and H. S. Isaacs, *J. Electrochem. Soc.*, 1996, **143**, 147.

34 H. Zhang, Y. Ye, R. Shen, C. Ru and Y. Hu, *J. Electrochem. Soc.*, 2013, **160**, D441–D445.

35 L. Wan, Z. Xu, Q. Xu, P. Wang and B. Wang, *Energy Environ. Sci.*, 2022, **15**, 1882–1892.

36 T. Chen, Y. Sun, M. Guo and M. Zhang, *J. Alloys Compd.*, 2018, **766**, 229–240.

37 T. Zhao, S. Wang, Y. Li, C. Jia, Z. Su, D. Hao, B. Ni, Q. Zhang and C. Zhao, *Small*, 2022, 2204758.

38 J. Zimou, K. Nouneh, R. Hsissou, A. El-Habib, L. El Gana, A. Talbi, M. Beraich, N. Lotfi and M. Addou, *Mater. Sci. Semicond. Process.*, 2021, **135**, 106049.

39 P. Djinović, J. Batista and A. Pintar, *Int. J. Hydrogen Energy*, 2012, **37**, 2699–2707.

40 R. Khatun, R. S. Pal, M. A. Shoeb, D. Khurana, S. Singhl, N. Siddiqui, M. K. Poddar, T. S. Khan and R. Bal, *Appl. Catal., B*, 2024, **340**, 123243.

41 X. Du, D. Zhang, L. Shi, R. Gao and J. Zhang, *J. Phys. Chem. C*, 2012, **116**, 10009–10016.

42 J. R. McBride, K. C. Hass, B. D. Poindexter and W. H. Weber, *J. Appl. Phys.*, 1994, **76**, 2435–2441.

43 J. Lin, L. Li, Y. Huang, W. Zhang, X. Wang, A. Wang and T. Zhang, *J. Phys. Chem. C*, 2011, **115**, 16509–16517.

44 A. Singhania, *Catal. Lett.*, 2018, **148**, 1416–1422.

45 Q. Zhang, Y. Wang, Y. Wang, A. M. Al-Enizi, A. A. Elzatahry and G. Zheng, *J. Mater. Chem. A*, 2016, **4**, 5713–5718.

46 W. Xiong, Z. Guo, H. Li, R. Zhao and X. Wang, *ACS Energy Lett.*, 2017, **2**, 2778–2785.

47 J. B. Wang, Y.-L. Tai, W.-P. Dow and T.-J. Huang, *Appl. Catal., A*, 2001, **218**, 69–79.

48 J. M. Sánchez-Amaya, G. Blanco, F. J. Garcia-Garcia, M. Bethencourt and F. J. Botana, *Surf. Coat. Technol.*, 2012, **213**, 105–116.

49 Z. Hu, X. Liu, D. Meng, Y. Guo, Y. Guo and G. Lu, *ACS Catal.*, 2016, **6**, 2265–2279.

50 A. Maradesa, B. Py, J. Huang, Y. Lu, P. Iurilli, A. Mrozinski, H. M. Law, Y. Wang, Z. Wang and J. Li, *Joule*, 2024, **8**, 1958–1981.

51 P. Xiao, W. Chen and X. Wang, *Adv. Energy Mater.*, 2015, **5**, 1500985.

52 M. Thommes, K. Kaneko, A. V. Neimark, J. P. Olivier, F. Rodriguez-Reinoso, J. Rouquerol and K. S. W. Sing, *Pure Appl. Chem.*, 2015, **87**, 1051–1069.

53 Z. Liang, D. Shen, Y. Wei, F. Sun, Y. Xie, L. Wang and H. Fu, *Adv. Mater.*, 2024, **36**, 2408634.

54 HYDROGEN SHOT: Water Electrolysis Technology Assessment, 2021.

55 T. Ling, D.-Y. Yan, H. Wang, Y. Jiao, Z. Hu, Y. Zheng, L. Zheng, J. Mao, H. Liu and X.-W. Du, *Nat. Commun.*, 2017, **8**, 1509.

56 Y. Pan, K. Sun, Y. Lin, X. Cao, Y. Cheng, S. Liu, L. Zeng, W.-C. Cheong, D. Zhao and K. Wu, *Nano Energy*, 2019, **56**, 411–419.

57 Y. Li, Y. Jiao, H. Yan, G. Yang, Y. Liu, C. Tian, A. Wu and H. Fu, *Angew. Chem., Int. Ed.*, 2023, **62**, e202306640.

58 X. Liu, Y. Yao, W. Li, Y. Zhang, Z. Liu, H. Yin and D. Wang, *Small*, 2024, **20**, 2308549.

59 Q. Qin, H. Jang, X. Jiang, L. Wang, X. Wang, M. G. Kim, S. Liu, X. Liu and J. Cho, *Angew. Chem.*, 2024, **136**, e202317622.

60 F. Ciucci and C. Chen, *Electrochim. Acta*, 2015, **167**, 439–454.

61 J. K. Nørskov, T. Bligaard, A. Logadottir, J. R. Kitchin, J. G. Chen, S. Pandelov and U. Stimming, *J. Electrochem. Soc.*, 2005, **152**, J23–J26.